Radio and Hard X-Ray Imaging Observations of the M 5.7 Flare of 2002 March 14

V.I. Garaimov[1], E.J. Schmahl[1,2], and M.R. Kundu[1]

[1]*Astronomy Department, University of Maryland, College Park, MD 20742*
[2]*Lab for Astronomy and Solar Physics, NASA Goddard Space Flight Center, Greenbelt, MD 20771*

ABSTRACT

We describe a flare of GOES class M5.7 which was observed simultaneously by RHESSI and NoRH (Nobeyama Radio Heliograph). The flare occurred in active region AR 9866 located near disk center. Both hard X-ray and microwave observations indicate that the flaring region consisted of a complex of multiple loops. In the microwave domain it clearly is of a class characterized by a double loop configuration: a small loop created by the emergence of a new flux interacting with an old flux, which is the main flare site, meaning that this is the site where we observe microwave, HXR, EUV emissions, and a remote flare site which is observed only in radio. In HXR there are clearly three loops, two of which have distinct foot points with co-located microwave source in one foot point; the third loop is large and filled with energetic electrons primarily emitting lower energy (12-25 keV) HXR. The successive energization of the loops gives the illusion of re-orientation with time of RHESSI flaring loops. There is a second peak in flaring emission in both microwaves and HXR, which also shows up as a short duration weak continuum in dynamic spectra (in the frequency range 30-500 MHz, 01:50-01:57 UT). Spectroscopic analysis of the RHESSI data shows that the spectrum can be fitted with a thick-target model with a thermal component and a broken power-law component. Viewed overall, the successive loops inferred from microwaves and HXR appear to show a decrease of magnetic shear as the flare proceeds.

Subject headings: Sun: corona — Sun: flares — Sun radio radiation — Sun: x-rays

1. INTRODUCTION

It has been known for a long time that flares occur in regions consisting of many magnetic loops and that a flare can be caused by the interaction between loops. Evidence of interaction between newly emerging flux and overlying magnetic fields causing flares have been provided from optical observations (see e.g. Zirin 1983; Kurokawa 1989), and soft X-ray observations from Yohkoh have provided evidence of interactions between coronal loops (e.g. Hanaoka 1994; Inda-Koide *et al.* 1995; Shimuzu *et al.* 1994). Only a limited number of observations of interacting flaring loops exist in the radio domain, primarily due to lack of good enough spatial resolution to demonstrate the existence of such interacting loops (see e.g. Kundu *et al.* 1982; Kundu & Shevgaonkar 1985). More recently because of observations made with the solar dedicated imaging radio telescope (NoRH) at 17 and 34 GHz, it has been possible to analyze a large number of flares and show evidence of interacting loops, although the spatial resolution was only of order $5'' - 10''$. Thus, Hanaoka (1996, 1997, 1999) and Kundu *et al.* (2001) provided evidence that emerging flux appeared near one sunspot- dominated active region and argued that interactions between this emerging flux and the overlying loop resulted in the onset of flares and microflares. The main flare site in each case was the location of emerging flux which was also the site of soft X-ray and EUV brightening. In addition the NoRH images showed that at 17 GHz a compact brightening occurred at the main flare site as well as at a remote region of opposite polarity. This observation obviously meant a double loop magnetic configuration of the flaring source, where high energy electrons generated or accelerated at the main flare site propagated over to the remote site producing microwave radio emission only.

In this paper we discuss a solar flare with similar magnetic field topology. Unlike previous papers dealing with double loop configuration, we have RHESSI imaging observations of hard X-rays of energy $\lesssim 100$ keV. Since RHESSI has more sensitivity and better spatial resolution than Yohkoh/HXT, it will be useful to check if the remote site of the double loop configuration does indeed produce only the radio emission or emit both radio and HXR emissions.

2. OBSERVATIONS

The flare was observed with the Nobeyama Radio Heliograph (NoRH) at 17 and 34 GHz and with the Ramaty High Energy Solar Spectroscopic Imager (RHESSI) in hard X-Rays in the energy range 6 - 100 keV. The flare event occurred on 2002 March 14, at 01:43 UT in the active region AR 9866.

The solar active region of interest, NOAA 9866, crossed the east limb on March 7, and gradually developed magnetic complexity (initially beta-gamma) as it moved toward the disk center. Intrusive polarity (a "delta" spot) appeared in its trailing region on March 12, and increased flaring followed in its vicinity. Further magnetic complexity (a second delta) appeared on March 13, and this led to a series of six M-class flares in the following week. The first of this series was an M5.7 flare that occurred at S11E10, peaking at 01:50 in soft X-rays on March 14. This flare was observed in hard X-rays by RHESSI during most of its rise and fall.

In the 12-30 keV band the flare started at 01:37 UT, peaked at 01:46 and continued after 01:54, the beginning of RHESSI night. RHESSI observed three minutes of the late decay phase (02:31-02:34), and in soft X-rays (GOES) the flare continued until at least 04:00. The radio emission was observed from about 01:40 UT and continued beyond 02:00 at which time the level of radio emission was still high (higher than the pre-flare level).

3.   RHESSI HARD X-RAY OBSERVATIONS

3.1.   Time Profiles

The time profiles of the flare in hard X-rays as observed by RHESSI in nine energy bands are shown in Fig 1. During the rise, count rates per detector exceeded 50,000 counts/s, (the point at which pulse pile-up becomes significant) and the first attenuator automatically switched in at 01:42:20. This is seen in the discontinuity of the time profiles in the lower energy bands. (The discontinuity has been approximately accounted for in computing the photon rate, but the finite width of the energy bands requires a complete treatment of the energy response matrix and modeling to eliminate the discontinuity altogether.)

The X-ray flux in the low energy bands (10-12, 12-15 keV) continued to rise for 3-4 minutes, but in the higher energy bands (24-92 keV), a number of impulsive bursts appeared at a mean cadence of 1 min, each burst lasting for 30-60 s.

3.2.   RHESSI Hard X-ray Imaging Observations

Cleaned images were made in nine energy bands (12-15, 15-19, 19-24, 24-30, 30-37, 37-45, 45-55, 55-75, 75-100 keV) for the period 01:36:30-01:37:30 and 01:41:00-01:54:00. Each map was based on 60-s integrations, with 2-arcsec resolution over a field of view (FOV) of 64"x64" (see Fig. 2).

The "pre-flare" source at 01:36 can be mapped only below ~ 19 keV. The source seen in a 3-minute map (01:36-01:39 UT, Fig. 2) has a single component, undoubtedly thermal. The first flare image set on the rise (01:40:00-01:41:00) shows a loop-like structure in the 12-15 keV band (Fig. 2), and this "loop" appears to be a continuous structure up to 55 keV. The center of the loop coincides with the pre-flare source seen 3-4 minutes earlier. In the next minute, (01:41:00-01:42:00) the spectrum hardens, and 3 isolated components appear at energies up to the 45-55 keV band. Maps above 55 keV at this time show little or no real structure because of poor photon statistics.

Subsequent maps start at 01:42:30, 10 s after the attenuator switched in. In the first post-attenuator map at the peak of the flare, the loop-like nature of the source appears at low energies, and two discrete components ("footpoints") appear above 19 keV. At this time, there are 3 footpoints visible in the 19-45 keV bands. The footpoint farthest to the southeast is visible only at this time, and only at energies up to ~ 45 keV. This particular footpoint coincides in time with the 1 GHz burst, and, as we note below, may be its manifestation in HXR. The other two footpoints are visible up to > 75 keV in the first 2 minutes. After 01:44:30 the double source seen in the 01:43:30-01:44:30 image in the 19-30 keV range appears "filled"in, remaining so until at least 01:51:30.

In the next higher band, 30-37 keV, the filling-in starts 1 minute later (01:45:30) and ends ~ 1 minute earlier. At higher energies the source appears double at all times after 01:41:00 (when it was triple). In the 55-75 keV band, the double source fades out at $\sim 01 : 47 : 30$, then reappears at 01:51:30 when the second largest burst of the flare occurs. During this burst, footpoints are visible at photon energies up to ~ 75 keV.

As a function of energy, the maps from 01:43:30 to 01:50:00 UT show a decrease of map quality with increasing energy. The cutoff above which good maps cannot be made decreases from about 75 keV to 55 keV after 01:43:30. In the maps at energies above 30 keV, there appears to be a clockwise re-orientation of the line between of the footpoint sources. Thus the eastern footpoint appears to move north and the western footpoint appears to move south. In view of the complex nature of the flare, possibly involving several loops, it is likely that new loops are being energized, which gives the appearance of re-orientation.

4. NORH RADIO OBSERVATIONS

The imaging radio observations were made with the NoRH at 17 and 34 GHz. We also made use of flux monitoring observations with NORP at 1, 2, 3.75, 9.4, 17 and 34 GHz. The NoRP time profiles at these frequencies are shown in Fig. 3. The main radio emission

has a rather broad peak at 01:43:40 UT at all these frequencies; the emission starts to rise slowly from about 01:42:00 UT. Note, however, that at 1 GHz there is a sharp peak at about 01:42:25 UT, with a correspondingly sharp rise of emission from 01:42:15UT; the emission with the broader peak (at 01:45 - 01:47 UT) starts to rise at 01:43:00 UT. This sharp peak at 1 GHz does not have any counterparts at higher frequencies. One can notice that the broader peak at around 01:42:40 slightly drifts to later times with decreasing frequency. The main flare emission including another significant peak at 01:52:30 UT lasts only about 15 min. In Fig 3 we show some RHESSI count-rate time profiles in the 12-25, 25-50, and 50-100 keV bands.

We studied the pre-flare radio emission (about 10 min. before the flare phase) at the flare site. Fig. 4 shows a TRACE image with MDI and 17 GHz contours around 01:41 UT. One can see some activity in the TRACE image, and a radio loop-like feature along the neutral line of the magnetic field in the flaring active region. Investigation of the MDI images near the main flare site shows the appearances of several opposite polarity delta-regions at the site, but none seems to be directly related to the triggering of the flare, if we consider the flaring loop configuration based upon radio data (see later).

Fig. 5b shows time plots of the magnetic field evolution around the main flare site. As one can see, the average magnetic field strength increased for positive polarity, but decreased for negative polarity. After the onset of the flare (marked by the dotted vertical line on the plots) the magnetic field strength changed abruptly. The peak magnetic field does not show big variations, but the minimum field decreased from -1350 G to -1650 G in course of the day of the occurrence of the flare. Similar behavior of the average magnetic field in the flare site was also observed in the case of the double-loop configuration of a flare observed on Oct. 25, 1999 by Kundu et al. (2001). [See also Wang et al. 2002, 2003; Kosovichev & Zharkova 2001]

Fig. 6a shows an MDI image along with 17 GHz intensity and polarization contours in the late flare phase (01:49:26UT). The radio contours show a double loop configuration of the flare, similar to what we observed in the case of the flare of Oct. 25, 1999 (referred to earlier). This configuration consists of a compact bipolar main flare site and a remote site observed in radio only, which is unipolar.

Figure 6b shows a TRACE image of the flaring region on which 17 GHz intensity contours are overlaid. The TRACE image does not clearly show the loop connection between the main and the remote sources. In figure 7 we present a set of main flare site TRACE images overlaid with 17 GHz polarization contours. During the beginning phase of the flare (from 01:42 to 01:50 UT) one can clearly see the double ribbon flare structure on the TRACE images. At later phases of the event we observed the development of the multi loop complex.

On these images left polarization contours correspond to the foot points (sunspot) polarity. The right polarization contours are located above the flaring loops.

5.   COMPARISON OF RHESSI HXR AND NORH MICROWAVE IMAGES

In section 2 above, we discussed the flare maps obtained by RHESSI. Figure 8 shows MDI images of the main flare site with superposed 17GHz contours and RHESSI HXR contours in the energy ranges from 12 keV to 100 keV. These contours represent X-ray emission during the maximum phase of the event. As one can see, at the main flare phase around 01:42:30 UT, the 12-15 keV contours correspond to the loop top emission and they have good agreement with the 17-GHz contours. The 15-19 keV, 19-24 keV contours correspond to the emission of the full long loop with SE-NW orientation. Also we are beginning to see emission from the footpoints of the main flaring loop. The higher energy contours mostly represent emission from the main loop footpoints. The 17 GHz contours lie in between the RHESSI foot points. This implies that the microwave emitting electrons (which are of higher energy than the HXR emitting electrons) fill up the main flaring loop with the foot points emitting only HXR emission. Fig. 8 indicates that there is a RHESSI HXR source in all the energy bands up to 100 keV corresponding to the spiky source at 1 GHz (see Fig. 3).

Upper limits on HXR for the secondary (western) NoRH source have been found, and they are essentially given by the sidelobe amplitudes in the maps. In Clean maps with "Clean boxes" around the locations of the main and western NoRH sources, using grids 4-9, these limits are $\sim 3\%, 6\%, 6\%$ and 3%, respectively, for the 3-6, 6-10, 10-19, and 19-200 keV bands. We have also found upper limits on the RHESSI HXR flux from the NoRH long loop by making maps that enhance the response to extended features and improve the statistics. To that end, we eliminated the finer grids 1-6 which would resolve out features shorter than $\sim 60''$ and put "Clean boxes" around the main source and the extended NoRH source. The upper limits are (again) given by the sidelobe amplitudes, $3\%, 6\%, 6\%$ and 3%, respectively.

Figure 9 shows an MDI magnetogram and 17-GHz V images and RHESSI contours at four different times (01:37:51, 01:42:30, 01:43:30, and 01:52:30 UT). The first time is pre-flare, and the next two correspond to times during the main flare peak. The last one corresponds to the time of the peak during the later phase of the event. One can visualize three different loops being involved in the flare process. One should note that at the time of the later peak (01:52:30), one of the higher energy (50-100 keV) foot points is located at one polarity (positive) of the 17 GHz polarized emission. This obviously defines one flaring loop. At 01:43:30 and 01:42:30 UT, one sees the same phenomenon, namely one of the foot points in the energy channel 50-100 keV overlies one polarity (positive) of the 17 GHz polarized

emission,but this polarity is located south of the previous 17 GHz positive polarity position. This defines the second flaring loop. Then there is the larger loop emitting 12-25 keV HXR without any well defined foot points, and the two end points lie outside of the previous RHESSI foot points. This defines the third loop. A possible fourth loop is suggested by the SE footpoint source seen in the RHESSI 15-37 keV bands at 01:42:30.

Using the NoRH maps of the flare we could calculate the time profiles of the radio emission at 17 and 34 GHz separately for the main and remote sources. Figure 10 shows time plots of intensity and polarization for the main and the remote sources. Analysis of these time profiles shows that the main source had mostly thermal emission except the emission during the peaks. The T_b spectral index reached a broad minimum between 01:44 and 01:45 UT, and in this time period, as we shall describe below, under the assumption of the bremsstrahlung mechanism, the emission measure must be very high ($> 10^{50}$). Fig. 11. shows the 17- and 34-GHz brightness temperature time profiles along with the derived spectral index. If the radio and HXR thermal sources have a common origin at this time, the radio optical depth must be of order unity. In fact, Fig 11 shows that the spectral index at 01:44-01:45 UT is $\sim 1.4 \pm 0.1$, which implies, again under the assumption of the thermal bremsstrahlung mechanism, that $\tau_{17} \sim 1.7$. For consistency, this requires specific values of the emission measure, density, and temperature in the HXR source, which we compute and compare in a later section.

The remote source had nonthermal emission and it was about 60% left circularly polarized. Inspection of the RHESSI maps shows no source at the remote site. This is, as discussed earlier, probably due to the limited dynamic range of the RHESSI images at the current state of calibration.

The main source had bipolar structure. And we calculate the time profiles of 17-GHz radio emission separately for the left and right circular polarities (Fig. 12). The western side of the main source was left circularly polarized with polarization degree of about 30%. This source represents mostly radio emission from the flaring loop footpoint. According to MDI images it is located above a sunspot. The eastern side of the main source was right circularly polarized with the polarization degree of less than 10%. The radio emission mostly originated from the eastern part of the main source.

Figure 13 shows 17-GHz polarization images of the flaring source and the distance between the maximum and the minimum of each image as a function of time. We do not observe any significant variation of the distance between the footpoints. At 01:52 UT the 17 GHz V image shows two right circularly polarized sources in the main flare site.

6. HARD X-RAY SPECTROSCOPY – RHESSI DATA

Spectroscopy using the Solar Software's "SPEX" (Schwartz *et al.* 2002) permitted us to make multi-parameter fits of a thick-target model to the photon spectra: temperature and emission measure of the thermal component, and flux and slope(s) of the non-thermal components(s) of the electron energy distribution. The fits to the photon spectra for one model using a single thermal component and a double non-thermal component are shown in Fig. 14 for the period 01:42:30-01:53:50.

The crosses show the background-subtracted data with error bars in flux and energy bandwidth. The triangles show the background that was subtracted. The light line shows the powerlaw components and the lines with dots show the thermal component. The background has been subtracted, but its contribution is significant only above ~ 50 keV, being ~ 2 orders of magnitude lower than the flare flux at 10 keV, 2-3 orders of magnitude smaller for the 20-40 keV range. The background is $< 50\%$ of the count rate for energies < 70 keV throughout the flare. The background was determined by examining the pre-flare period and other like orbits, there being no post-flare data in the flare orbit. For the purposes of this paper, the background in each energy band was taken to be constant, equal to the mean pre-flare count rate in the 01:14-01:18 time range.

The model used to fit the data is an isothermal plus broken power-law electron distribution with lower and upper cutoffs. The model, described by Holman (2001), Holman *et al.* (2003), is determined by computing thick-target bremsstrahlung from a multi-parameter distribution in 20-s time bins throughout the flare. The initial model has 8 parameters: emission measure (EM), temperature (T), thick-target electron flux (a_{norm}), power-law index (δ_1) below the energy break E_{brk}, upper power-law index (δ_2), and lower and upper cutoffs (a_{cutoff}, b_{cutoff}). Fits made with all 8 parameters free show that the upper index $\delta_2 > 5$, meaning that the fits should be only marginally affected by the upper cutoff. This is borne out by fits with $b_{cutoff} = 400$ and 2000 keV, which show no significant difference. Only a lower limit on b_{cutoff} can be found: $b_{cutoff} \sim 400$ keV, and in subsequent fits we have fixed b_{cutoff} at this value. The break energy E_{brk} is not well determined throughout the flare, since the spectral shape above 25 keV goes from concave upwards ($\delta_1 < \delta_2$) early in the flare to concave downwards ($\delta_1 > \delta_2$) later on, and to concave upwards again in the late phase of the flare. This means that the break energy is indeterminate twice in the flare. We have therefore taken the break energy to be constant at 40 keV. (Its mean value in the 7-parameter fits is 39 ± 13 keV.) The resultant fits with 6 free parameters are not significantly different in quality as measured by the χ^2 statistic.

In general, the lower cutoff does not show significantly better fits as measured by χ^2 when it is changed from 10 to 20 keV. We have therefore done 5-parameter fits (2 thermal

and 3 non thermal) for $a_{cutoff} = 10$ and 20 keV. The χ^2 statistic is less than 1 for all time intervals with either cutoff.

We have tried fits without a non-thermal break (4-parameter fits), and find poor fits. The mean value of χ^2 is 3 times larger than for the 5 or 6-parameter fits, and $\chi^2 > 2$ for the first 2 and the last 2 minutes of the flare. This indicates that the break energy is real and must be included in the parameterization. It is possible, however, that a double thermal source with a power-law thick-target model could fit the data equally well. We have not explored this possibility because it would not change the estimates of electron numbers or the energetics significantly. There is a degree of diminishing returns in any attempts to improve this model, since there is always considerable non-uniqueness in inverting bremsstrahlung spectra (Brown and Emslie, 1988, Holman, 2003).

7. DISCUSSION

We have observed a flare of importance M5.7 using RHESSI in hard X-rays and NoRH at 17 and 34 GHz simultaneously. The flaring source in microwaves clearly exhibits a double loop configuration similar to what we observed for a flare on October 25,1999 and several other flares (Kundu *et al.* 2001, Kundu and Garaimov 2003). At the main flare site the microwave source has two distinct oppositely polarized components, which must delineate a small loop. The remote source which is connected to the main flare site by a large loop is seen only in radio, obviously due to a stronger magnetic field. Even with RHESSI's high sensitivity one does not observe HXR at the remote site. Hard X-ray emitting sources are observed by RHESSI only at the flare site. (This may be the result of a finite dynamic range, which with the present calibration is limited by sidelobes of 3-6%.)

The RHESSI HXR sources consist of at least three loops – two small loops with different north-south orientations at the eastern side, which are populated primarily by high energy electrons (radiating 50-100 keV photons), as manifested by distinct foot points for both loops at these energies. In each loop, only one of the RHESSI foot points has a co-located microwave source, implying that both small loops have asymmetrical magnetic field structure. The 17 GHz source is located in between the two RHESSI foot points in high energy bands (50-100 keV), which suggest that microwave emitting electrons must fill up the whole loop. The third longer loop is populated by lower energy electrons as evidenced by 12-25 keV photons. Note that during the impulsive peaks the microwave emission is mostly produced by higher energy electrons via the gyro-synchrotron mechanism, whereas the hard X-ray emission is produced by bremsstrahlung. Between the peaks, however, as mentioned earlier, a significant fraction of the radio emission may be thermal, and we can determine

whether the radio and HXR have a common origin at those times.

It is of interest to compare the electron spectra fitted to the RHESSI HXR data, but it is not feasible to make images that distinguish the spatial features of each component at all energies and at all times. However, isolated images in Fig. 2 show the main features of each component. Inspection of the spectral fits (Fig. 14) reveals that in certain bands and time ranges, a single one of the components dominates. Using these model fits, we have identified the time intervals and bands during which one component radiates $\geq 90\%$ of the total band flux. The thermal component morphology is shown by the 12-15 keV maps for 01:43:30-01:53:30, where the source is elongated and single. The non-thermal component is shown by the maps for 37 keV and higher in the same time period.

We have used the thick-target model to determine the thick-target electron flux $\Phi(E, t)$. Integrating the loss rate $\Phi(E, t)$ over energy from the lower cutoff ($a_{cutoff} = 10$ or 20 keV), we get the rate of electron loss, $\Phi(t)$, in the target. Actually, the upper limit of the integration is not known, except that it must be at least ~ 400 keV, which, roughly, is where the precipitating electrons radiate 200 keV photons, the highest energy with spectral information.

Fig. 14 (lower left panel) shows the results of computing $\Phi(t)$. For $a_{cutoff} = 10$ keV, $\Phi(t)$ ranges from 2×10^{35} to 2×10^{36} electrons/s, and for $a_{cutoff} = 20$ keV, $\Phi(t)$ ranges from 2×10^{36} to 2×10^{38} electrons/s. The number of non-thermal electrons, N_{NT}, is determined by integrating $\Phi(t)$ over time. For a 20-keV lower cutoff, we find this to be (upper curves in the bottom left panel) $N_{NT} = 8 \times 10^{38}$, and for a 10-keV cutoff, $N_{NT} = 5 \times 10^{40}$.

The energy distribution loss rate $P(E, t)$ is computed from $\Phi(E, t) \cdot E$, and the energy loss rate $P(t)$ is found by energy integration. These are shown in Fig. 14. The time- and energy-integrated electron loss for a 20-keV lower cutoff is 1×10^{31} ergs, and for a 10-keV lower cutoff, 4×10^{32} ergs.

For a source volume V, the total number of thermal electrons is $N_{therm} = \sqrt{(EM\,V q)}$, where q is the fill-factor, assumed to be unity. For a cylindrical volume of diameter $10''$ and length $30''$, $V = 8.8 \times 10^{26}$ cm^3, compatible with the maps, and EM$=2 \times 10^{49}$, we find $N_{therm} = 1.3 \times 10^{38}$. This is of the same order as the total number of non-thermal thick-target electrons estimated from our model assuming a 20 keV energy cutoff, $N_{NT} = 8 \times 10^{38}$. With a 10 keV cutoff, N_{NT} is about 2 orders of magnitude higher, while the thermal source remains about the same.

The total thermal energy from the RHESSI data (using the same volume and emission measure as above, and $T = 2.2$ keV) is $3kT\sqrt{EMV} = 1.4 \times 10^{30}$ erg. (The thermal energy derived from the GOES data is about 20% higher.) This is about an order of magnitude smaller than the estimate of the time- and energy-integrated electron loss for a 20-keV lower

cutoff. This shows the well-known excess of the non-thermal energy over the inferred thermal energy ~ 10 keV (Dennis *et al.* 2003)

It is of interest to compare the HXR numbers with those inferred from the radio observations. The upper electron spectral index inferred from hard X-rays is $\delta \sim 5.5$. We assume that this spectral index is the same at MeV energies, where electrons contribute most of the gyrosynchrotron emission. If the source is optically thin at 17 and 34 GHz, then the brightness temperature is proportional to the emissivity η_ν: $T_b = (c^2/k\nu^2)\eta_\nu L$. We assume that the radiating volumes are identical in hard X-rays and microwaves, and that $L \sim 5Mm$, so that $T_b = 1.1 \times 10^{25}\eta_\nu$ at 17 GHz. From Dulk and Marsh 1982, we estimate the dependence of η_ν on magnetic field (B), density (N), δ and ν. The non-thermal electron density is 2×10^9 in the first minute of the flare, given the volume used earlier, and a 20-keV cutoff. (For the 10 keV cutoff it is 10 times higher.) At frequencies much greater than the gyrofrequency, and with $\delta = 5.5$, Dulk and Marsh's expressions yield:

$$\eta_\nu = 1.5 \times 10^{-27} BN(\nu/\nu_B)^{-3.73} \qquad (1)$$

where we have assumed that the angle relative to the magnetic field is 45°. The strong dependence on magnetic field through the gyrofrequency $\nu_B (= 2.8 \times 10^6 B)$ means that there is considerable uncertainty in estimating N from η_ν and T_B.

If the source is optically thin, the magnetic field necessary to match hard X-rays and radio at the start of the flare, when $T_b(17$ GHz$) = 8 \times 10^7$ K, is ~ 1000 G. At such high field strengths, the approximation assuming $\nu << \nu_B$ breaks down. But also the optical depth $\tau \sim 0.2$, which means that the observing frequencies are near the spectral peak. This is consistent with the fact that throughout the flare the 17-34 GHz spectral index is less than 3, which, in turn, is less than the mean 5.5 HXR spectral index (Fig 14). Alternatively, the electron spectrum might flatten at energies beyond RHESSI's range. If that is the case, then smaller magnetic fields (~ 100 G) would suffice, and the electron density might be orders of magnitude smaller than the HXR-emitting electrons. But, to carry the argument farther, the flattening of the radio spectrum to $\delta \sim 1.5$ two minutes from the flare start is impossible to explain in terms of a spectrum without an upper cutoff.

The flattening is also not explained, as suggested earlier, in terms of a thermal radio source, because that would conflict with the HXR emission measures ($< 2 \times 10^{49}$) and temperatures ($< 30MK$). The minimum emission measure required to make the thermal source optically thick ($\tau_{17} > 1$) is 2×10^{51} cm^{-3} for a temperature of 40 MK at the 01:44 minimum in the spectral index shown in Fig. 15. Thus the flattening must be interpreted in terms of a changing gyrosynchrotron spectrum, where the spectral maximum moves up

close to or above 17 GHz.

8. CONCLUSIONS

We have found that the HXR thermal component agrees in size and location, but has lower temperature and inferred density than the Nobeyama 17 GHz source at times when its spectral slope is flattest, and when non-thermal electrons are expected to have the smallest contribution. It is interesting to note that the 2002 July 23 X-flare shares this characteristic. (Holman *et al.* 2003, White *et al.* 2003). The 17- and 34-GHz emissions were inferred to be fully non-thermal for the July 23 event. As mentioned by Holman (2003), Silva *et al.* (2000) found that the microwave spectrum (from OVSA) is often flatter than expected based on hard X-ray spectra (from BATSE). Our estimates of the density of the thermal and non-thermal electrons show that consistency between radio and hard X-rays requires quite strong ($\sim$ 1000 G) magnetic fields in the flare structures.

We find that there are several loop structures in the flare, some of them not seen in hard X-rays, at least with RHESSI's present data-analysis capabilities. The HXR sources consist of at least three loops – two small loops with different north-south orientations at the eastern side, and these are energized sequentially during the flare. The simplest explanation for the appearance of the remote source seen in radio without HXR is that it has a stronger magnetic field. The formation of new loops as inferred from the microwave and HXR images seems to follow a pattern in which loops become less parallel to the flare ribbons and more oriented perpendicular to them. Such a pattern was seen in the 2000 July 14 flare (the "Bastille Day" flare), where HXT observations of loop footpoints suggested that the magnetic loops went from a highly sheared state to a less sheared state during the course of the flare (Masuda, Kosugi, and Hudson, 2001, Somov et al, 2002). In this case, no clear evidence was seen for diminishing footpoint separation (as seen in the "Bastille Day" flare), but the orientation of successive loops follows the same pattern, which Somov *et al.* interpret as the result of relaxation of magnetic tension generated by photospheric shear flows.

9. ACKNOWLEDGMENTS

REFERENCES

Brown, J., & Emslie, A.G.: ApJ **331**, 554, 1988.

Dennis, B., Veronig, A., Schwartz, R., Sui, L., Tolbert, A., Zarro, D. & the RHESSI Team, Adv. Spa. Res. **32**, No. 12, 2459, 2003.

Dulk, G. & Marsh, K.: Sol. Phys. **111**, 113, 1982.

Garcia, H.: Sol. Phys. **154**, 275, 1994.

Holman, G.: http://hesperia.gsfc.nasa.gov/hessi/flarecode/bremthickdoc.pdf, 2001.

Holman, G.: ApJ **586**, 606, 2003.

Holman, G., Sui, L., Schwartz, R. & Emslie, G. A.: ApJ **595** L97, 2003.

Hanaoka, Y.: ApJ **420**, 37, 1994.

Hanaoka, Y.: Sol. Phys. **165**, 275, 1996.

Hanaoka, Y.: Sol. Phys. **173**, 319, 1997.

Hanaoka, Y.: in Nobeyama Symp., Solar Physics with Radio Observations, eds. T. Bastian, N. Gopalswamy & K. Shibasaki (Tokyo: Nobeyama Radio Obs.), 229, 1999.

Inda-Koide, M., Sakai, J., Kosugi, T., Sakao, T., & Shimizu, T.: PASJ**47**, 323, 1995.

Kosovichev, A., & Zharkova, V.: ApJ **550**, L105, 2001.

Kundu, M. R., Grechnev, V., Garaimov, V., & White, S.: ApJ **563**, 389, 2001.

Kundu, M. R. & Garaimov, V.: Adv. Spa. Res. **32**, No. 12, 2497, 2003

Kundu, M. R.; Schmahl, E. J.; Velusamy, T.: ApJ **253**, 963, 1982.

Kundu, M. R. & Shevgaonkar, R.: ApJ **297**, 644, 1985.

Kurokawa, H.: Space Sci. Rev. **51**, 49-84. Oct. 1989.

Masuda, S., Kosugi, T., & Hudson, H.: Sol. Phys. **204**, 55, 2001.

Schwartz, R., Csillaghy, A., Tolbert, A., Hurford, G., McTiernan, J., Zarro, D.: Sol. Phys. **210**, 165, 2002.

Shimuzu, T., Tsuneta, S., Acton, L., Lemen, J., Ogarwara, Y., & Uchida, Y.: ApJ**422**, 906, 1994.

Silva, A., Wang, H., & Gary, D.: ApJ **545**, 1116. 2000.

Sui, L.; Holman, G.; Dennis, B.; Krucker, S.; Schwartz, R., Tolbert, K.: Sol. Phys. **210**, 245, 2002.

Somov, B., Kosugi, T., Hudson, H., Sakao, T., & Masuda, S.: ApJ **579**, 863, 2002.

Thomas, R. J.; Crannell, C. J.; Starr, R.: Sol. Phys. **95**, 323, 1985.

Wang, H., Ji, H., Schmahl, E., Qiu, J. Liu, C. Deng, N.: ApJ **580**, L177, 2002.

Wang, H.: BAAS **34**, 23.03, 2003.

White, S. M., Krucker, S.; Shibasaki, K.; Yokoyama, T.; Shimojo, M.; Kundu, M. R.: ApJ **595**, L111, 2003.

Zirin, H.: ApJ **274**, 900, 1983.
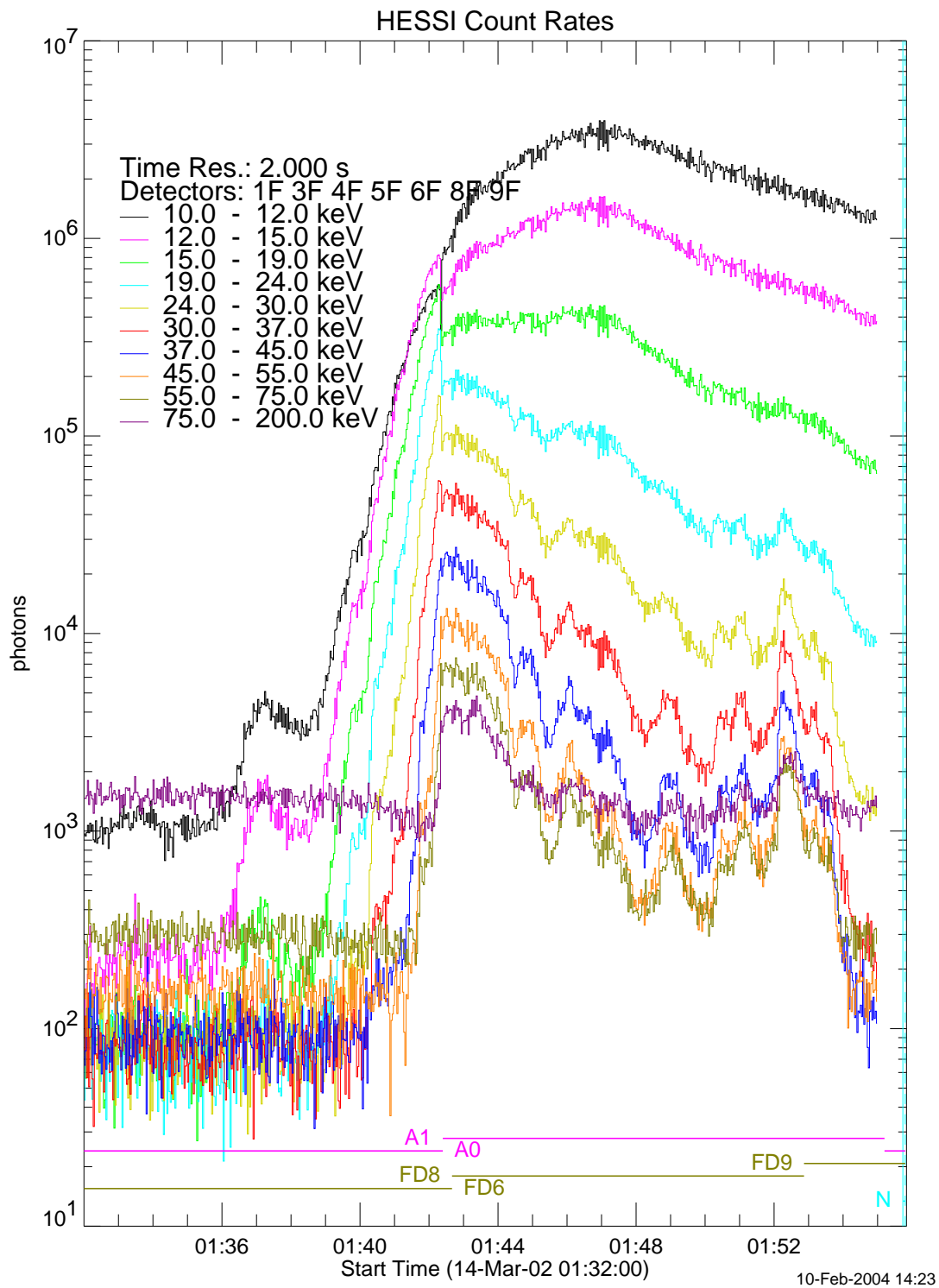
Fig. 1.— Time profiles of RHESSI hard X-rays in 10 energy bands
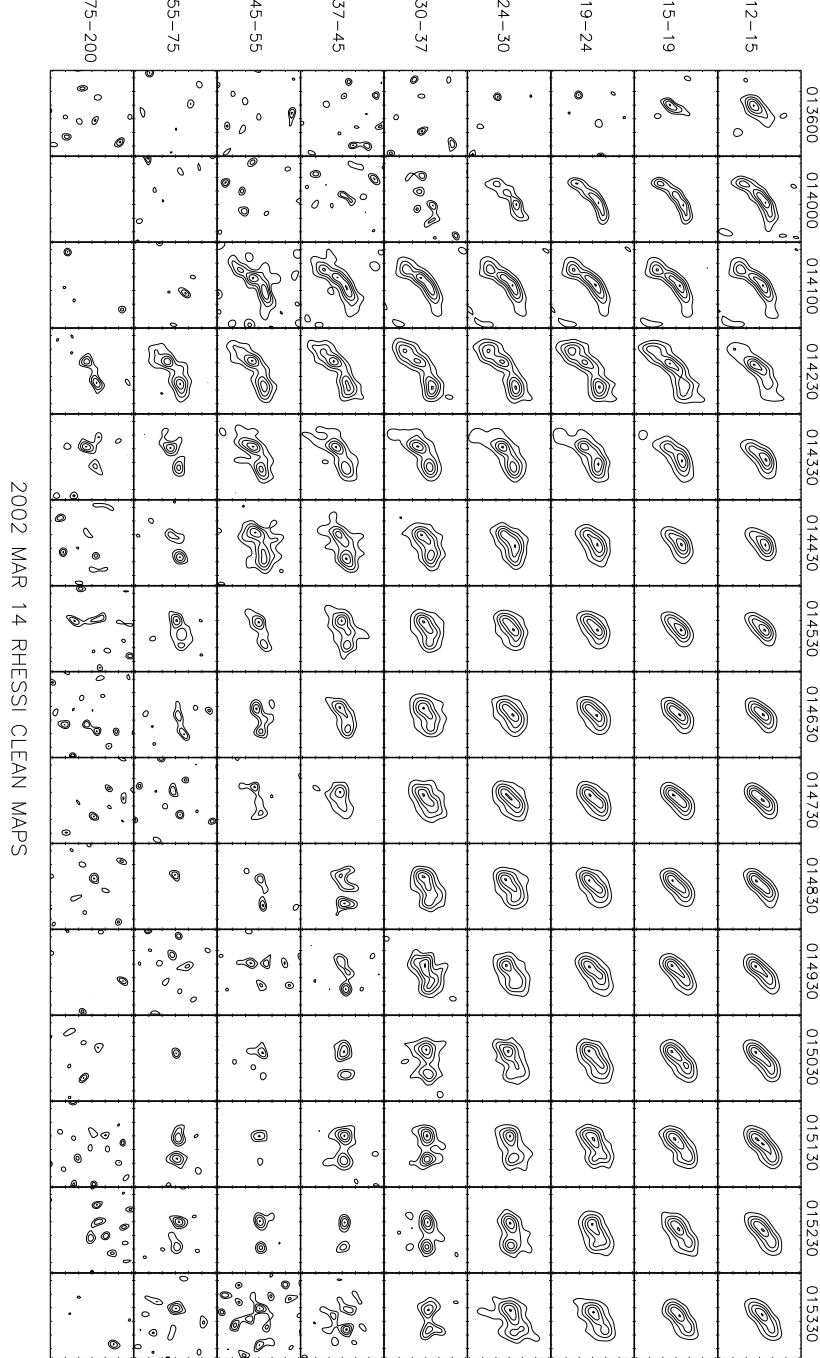
Fig. 2.— RHESSI narrow-band images of the flare. The 13 columns show Clean maps over a $64 \times 64''$ field of view with $12''$ pixels. The contours at the energies below 37 keV are at 20, 40, 60, 80 and 99% of the map maximum. At higher energies the lower contours are deleted for clarity.
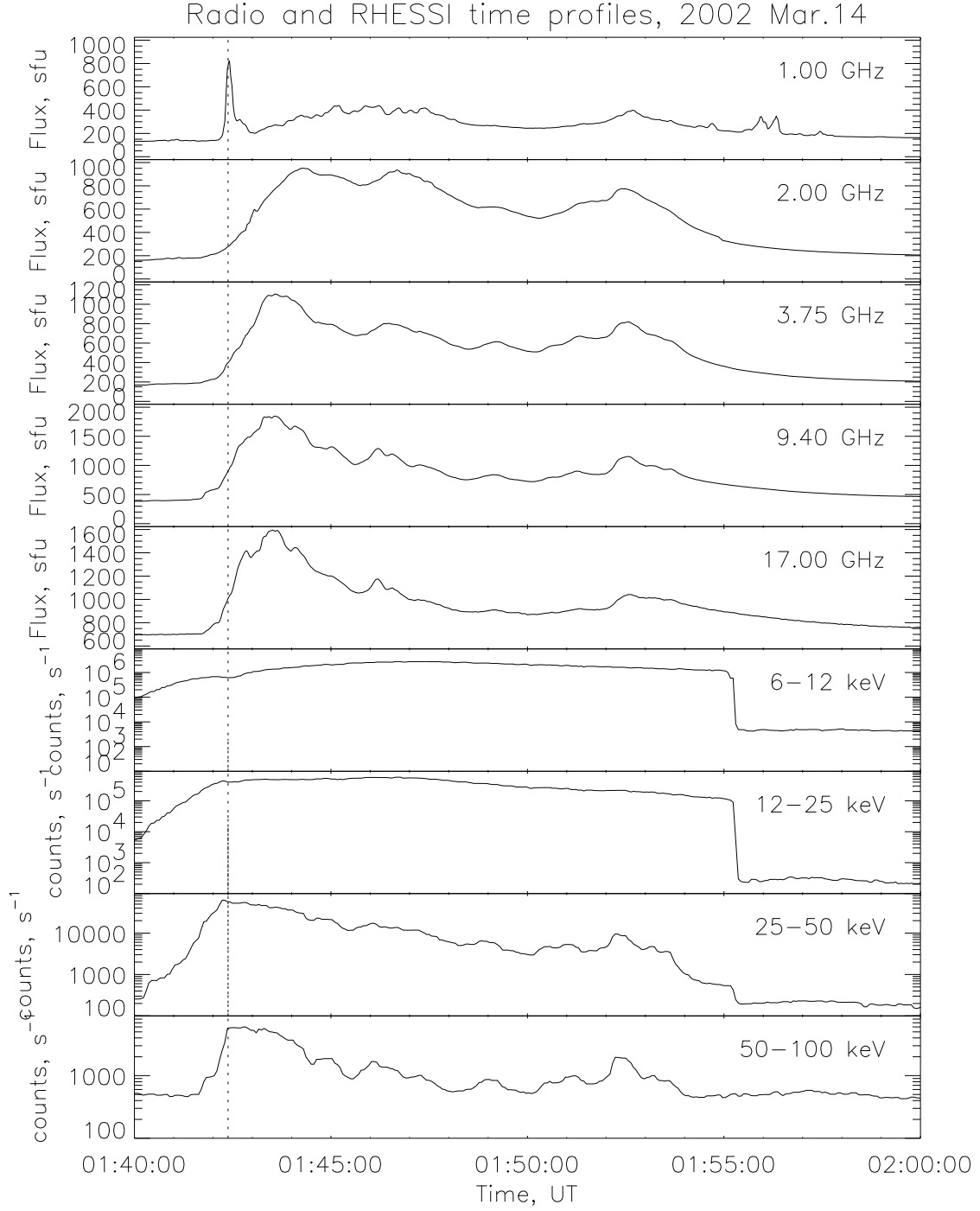
Fig. 3.— Time profiles of the total flux from the Nobeyama polarimeter and heliograph and the RHESSI HXR count rate
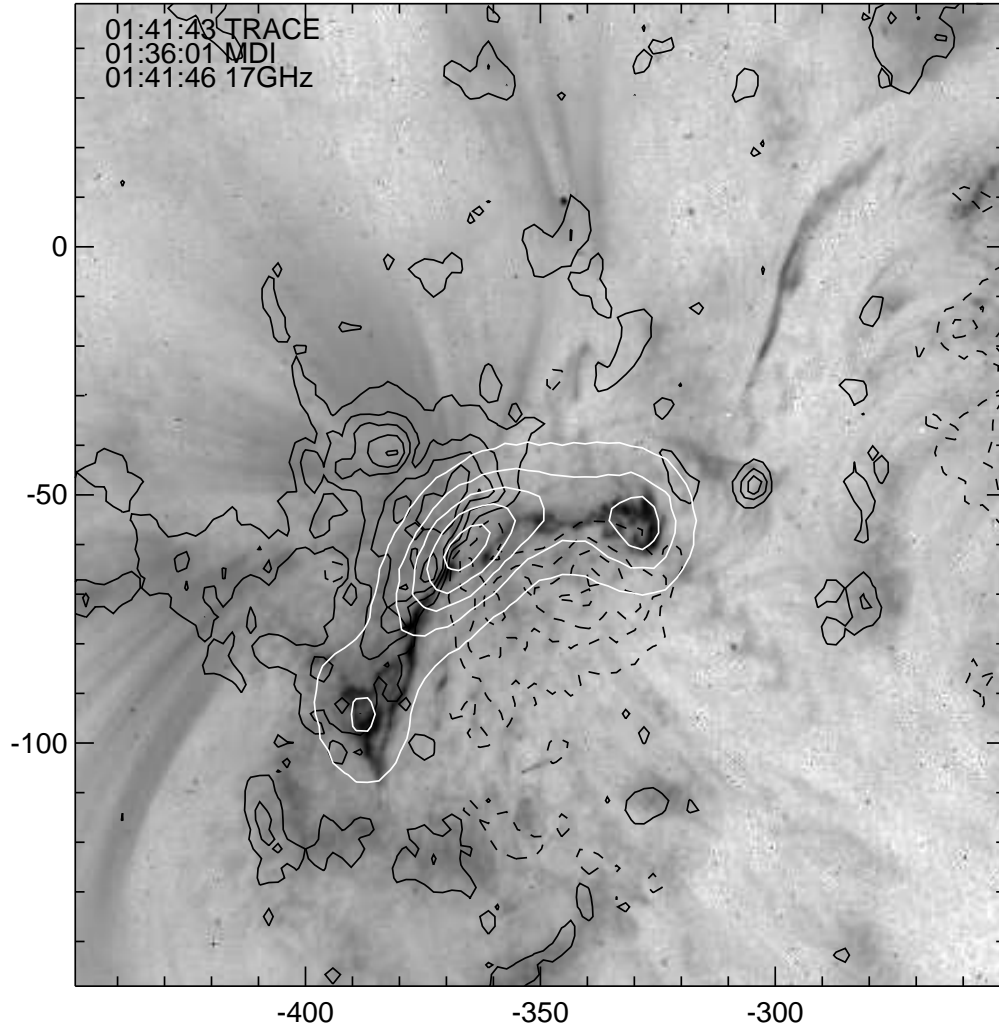
Fig. 4.— TRACE image with MDI and 17 GHz contours around 01:41 UT.
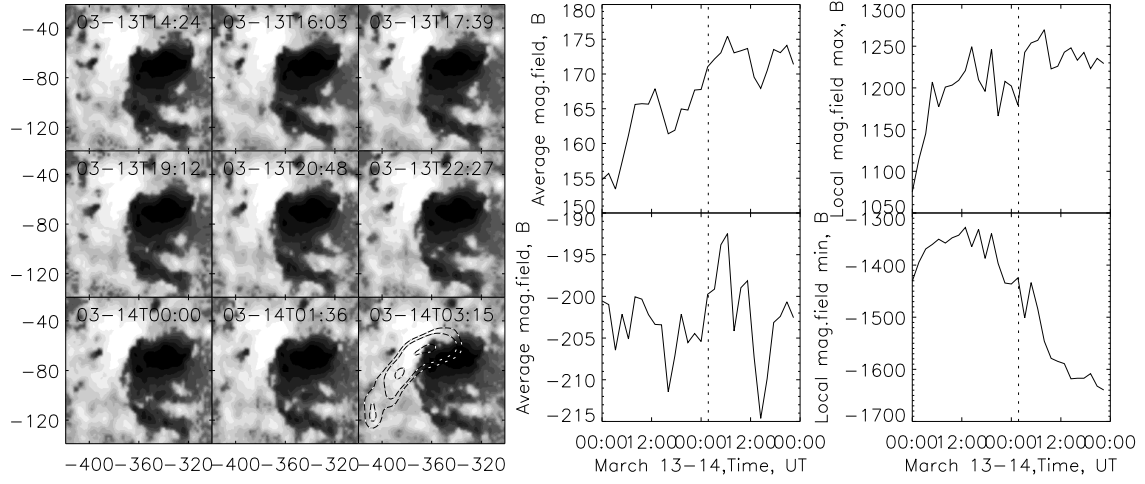
Fig. 5.— (a) Images of the photospheric magnetic field from MDI near the main flare site showing the appearances of several opposite polarity delta-regions at the site' (b) plots of average positive and average negative fields and maximum and minimum magnetic fields preceding and following the onset of the flare.
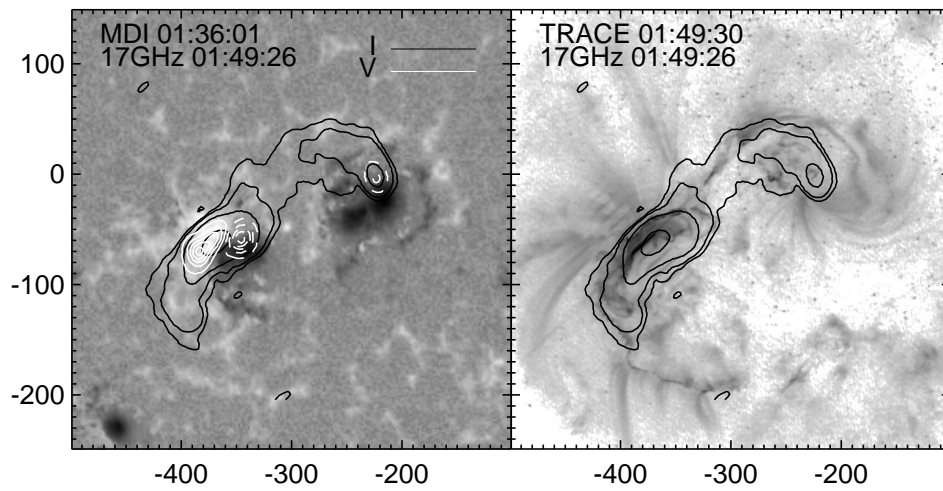
Fig. 6.— 17 GHz map (contours) superposed on (a) an MDI magnetogram and (b) a TRACE 195 A image. Black solid contours–I (total intensity); white solid contours–positive V; white dashed contours–negative V.
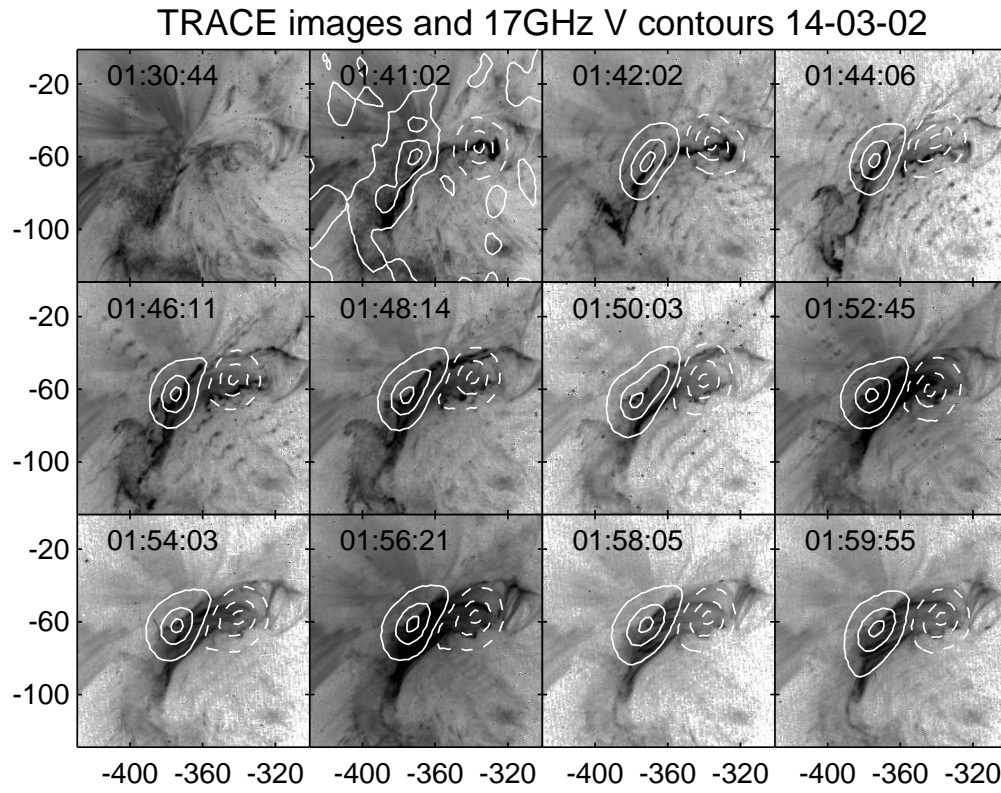
Fig. 7.— TRACE images and 17 GHz V contours (solid–positive; dashed–negative).

MDI image and 17GHz and HESSI contours 2002-03-14T01:42:30
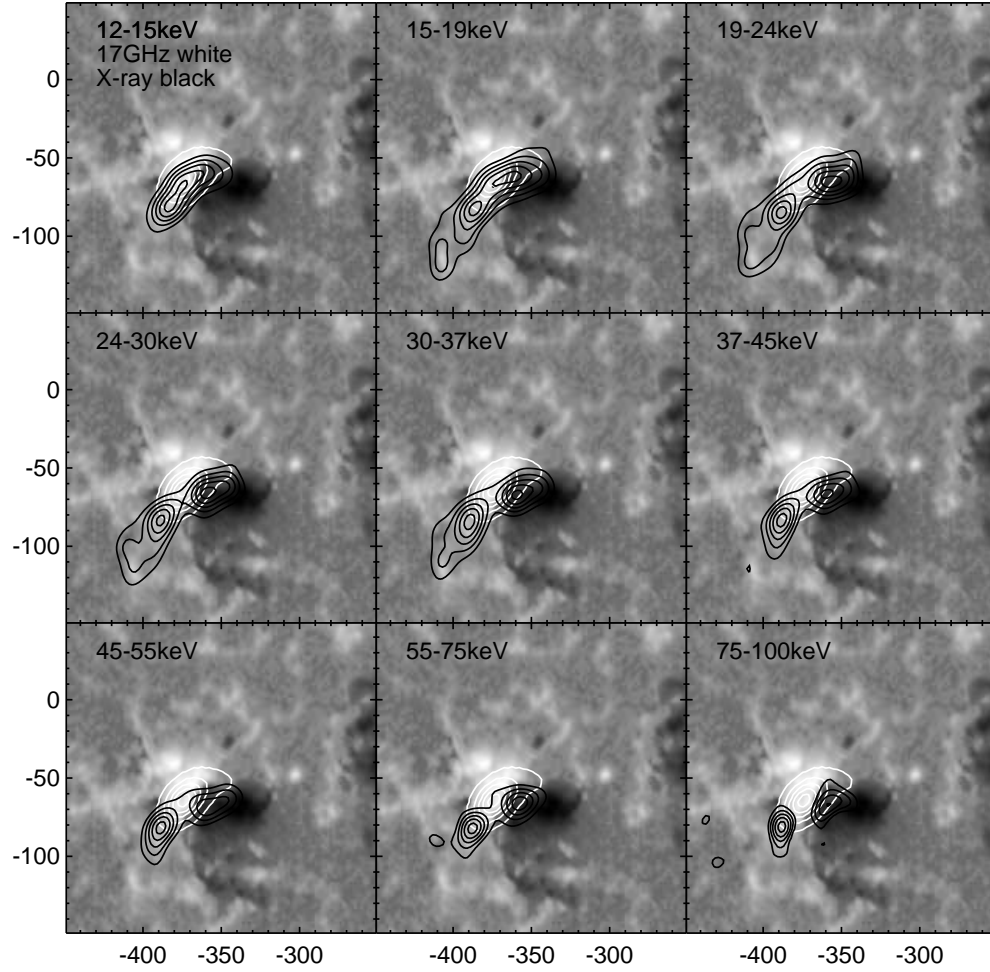
Fig. 8.— MDI magnetogram with superposed 17 GHz contours (white) and RHESSI HXR contours (black).
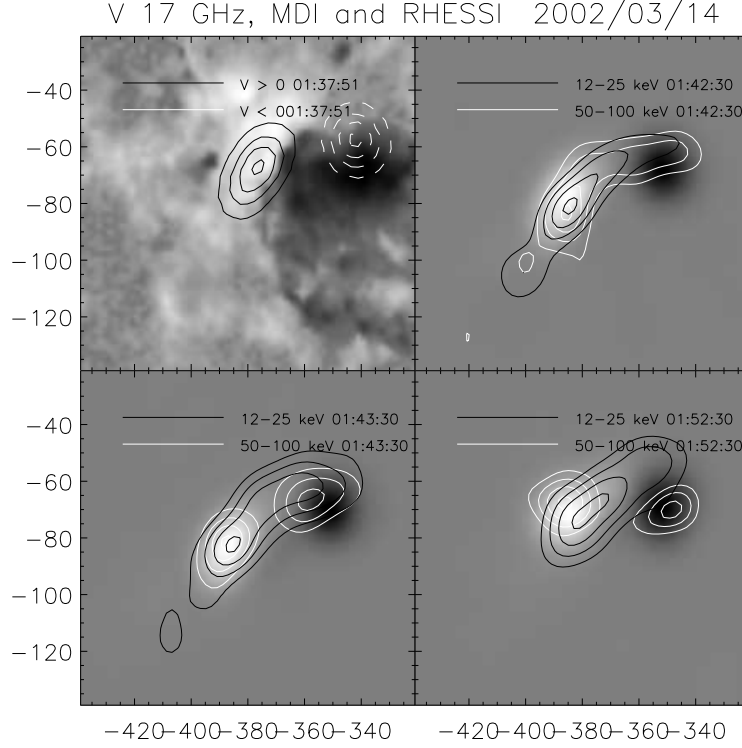
Fig. 9.— Top-left panel: Polarized intensity V (17 GHz) for 01:37:51 superposed on an MDI magnetogram at 01:36:30. Other panels: RHESSI 50-100 keV (white) and 12-25 keV (black) contours superposed on polarized intensity V(17 GHz) images at 01:42:30, 01:43:30 and 01:52:30. Note the change in orientation of the 50-100 keV footpoints relative to the 12-25 keV loop at 01:52:30.
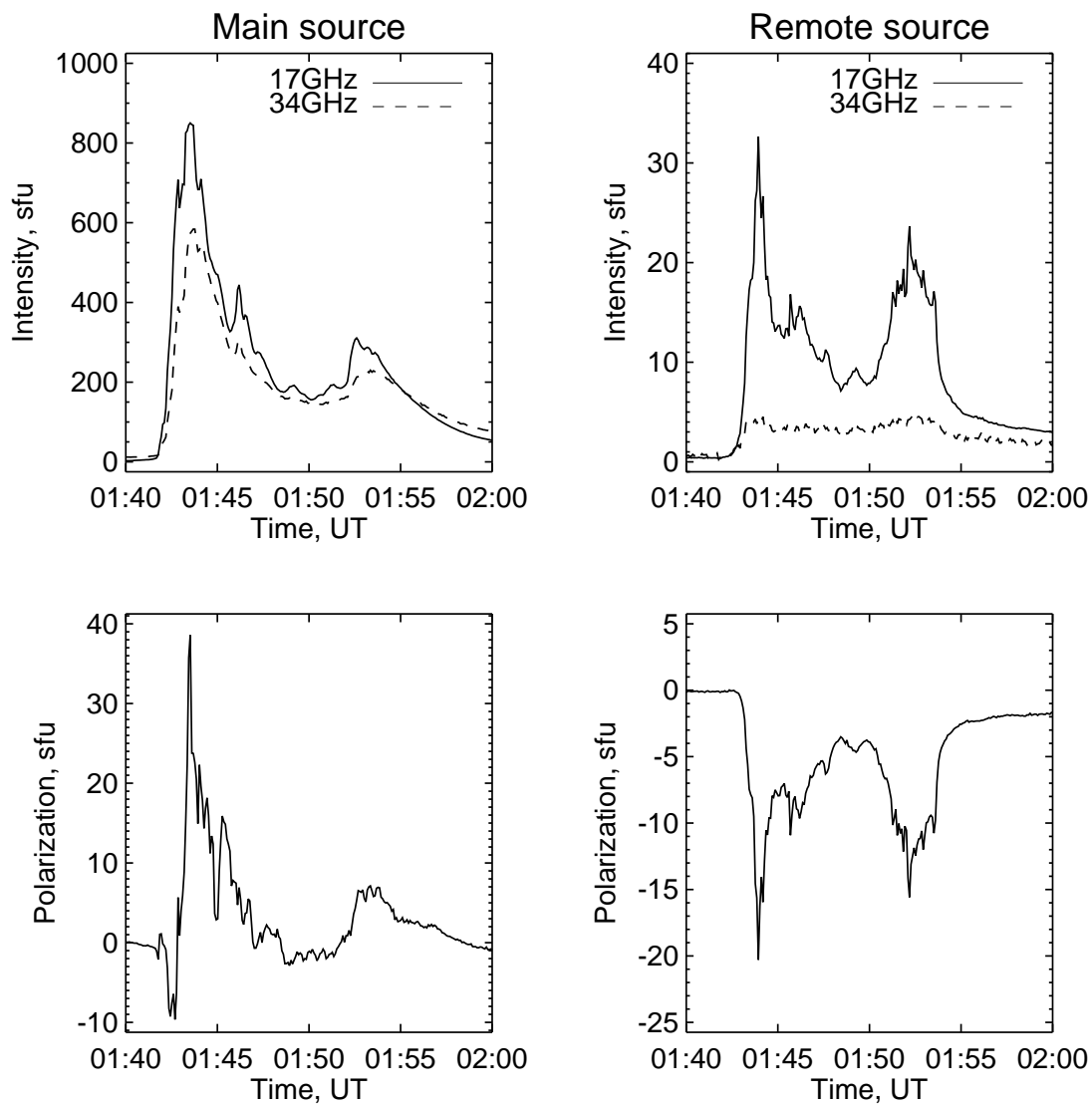
Fig. 10.— Radio I and V time profiles of the main source and remote source. The remote source has a similar time profile to the main source, except that it is oppositely polarized.
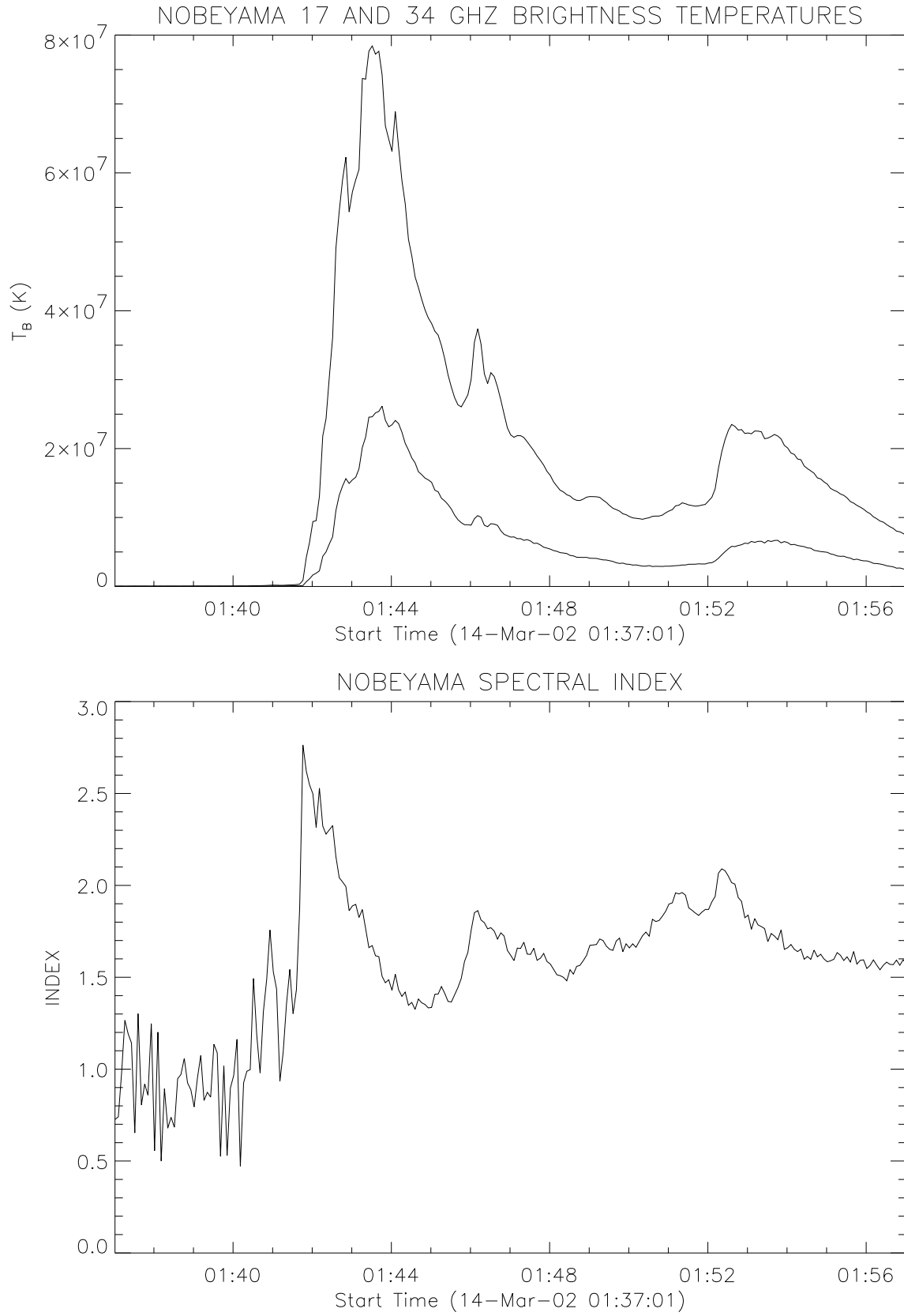
Fig. 11.— Brightness temperature profiles at 17 and 34 GHz, and the derived spectral index.
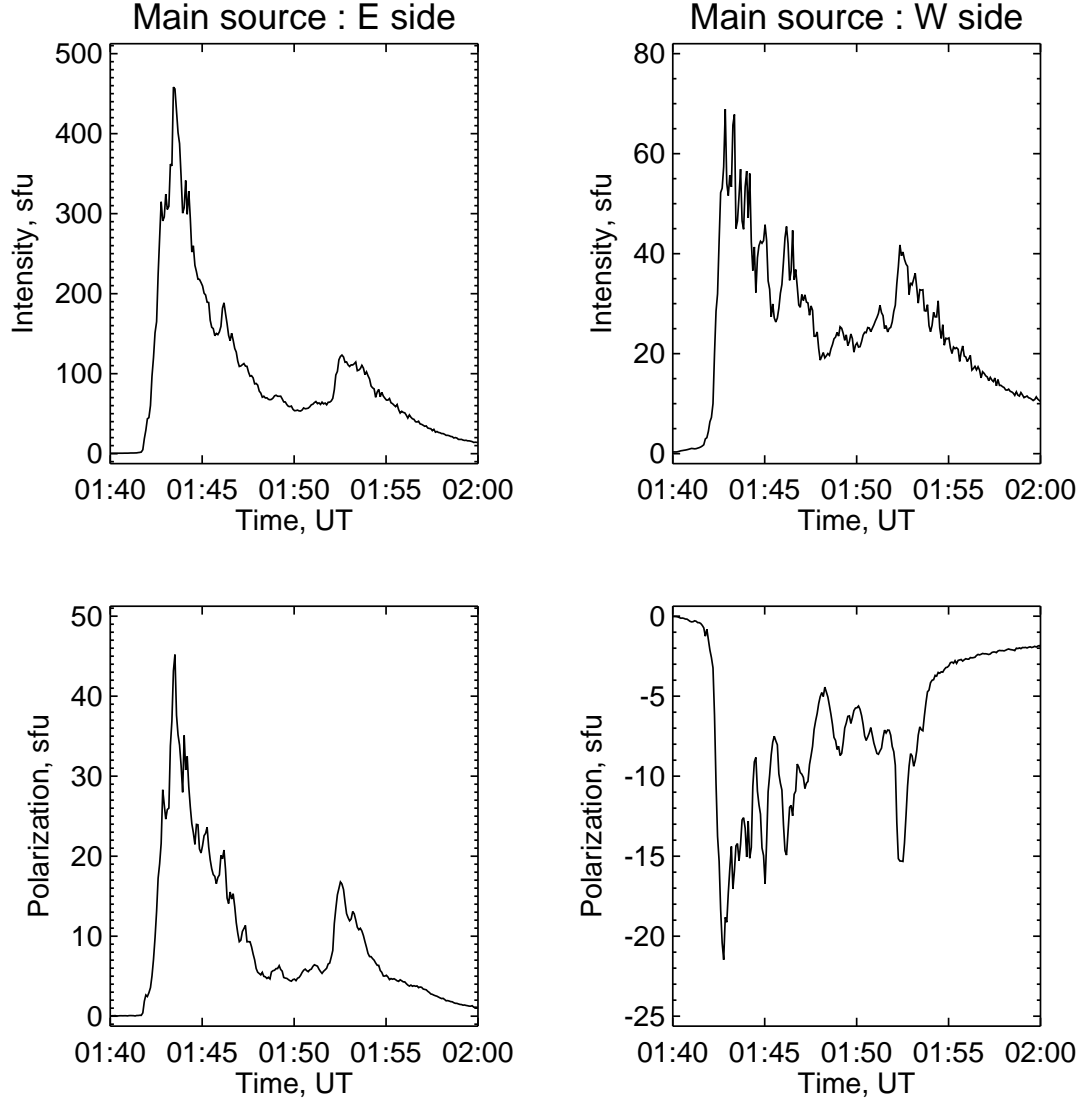
Main source : E side

Main source : W side

Fig. 12.— 17 GHz time profiles of the east and west sides of the main source.
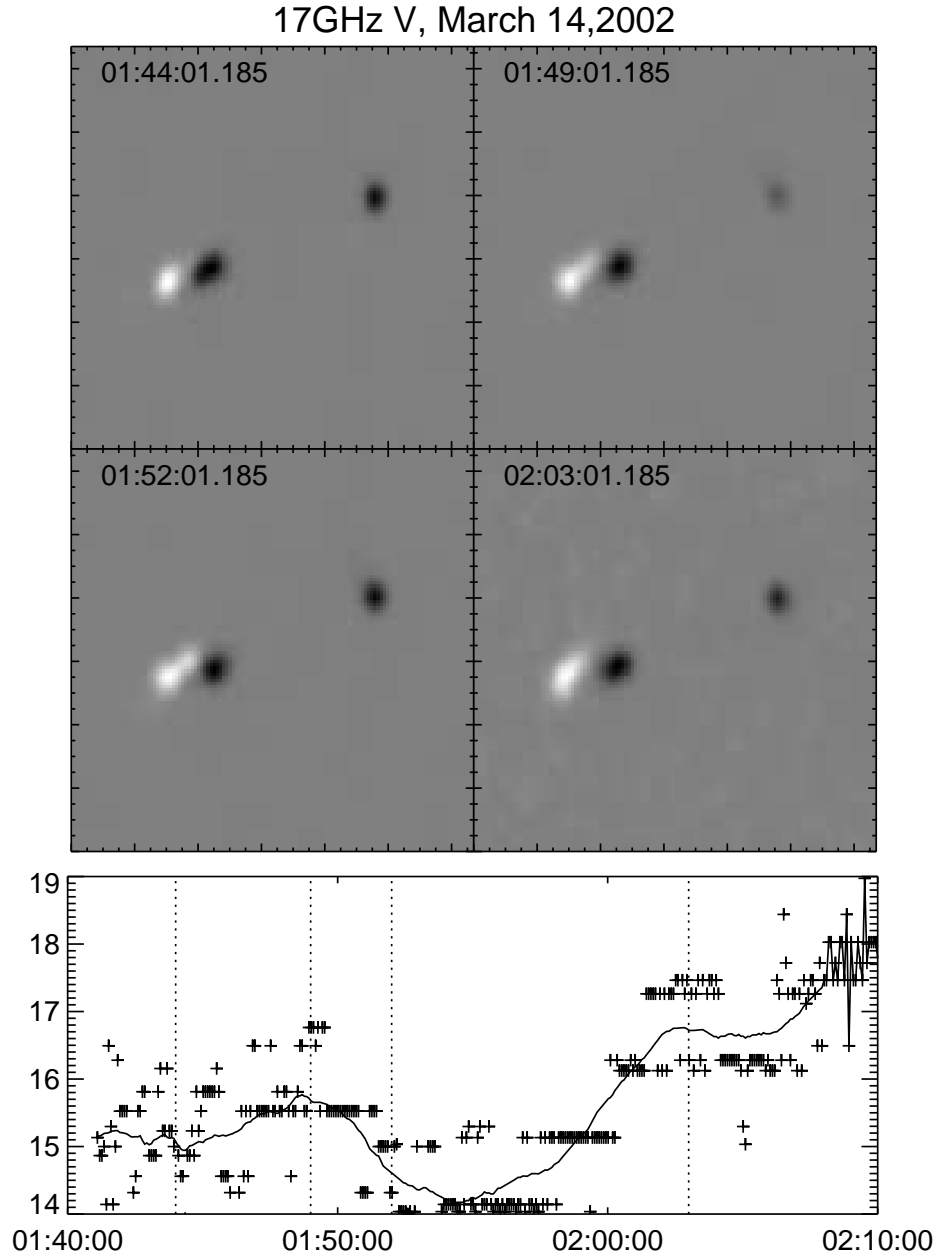
Fig. 13.— 17-GHz polarization images of the flaring source and the distance of separation between the maximum and the minimum of each image as a function of time.
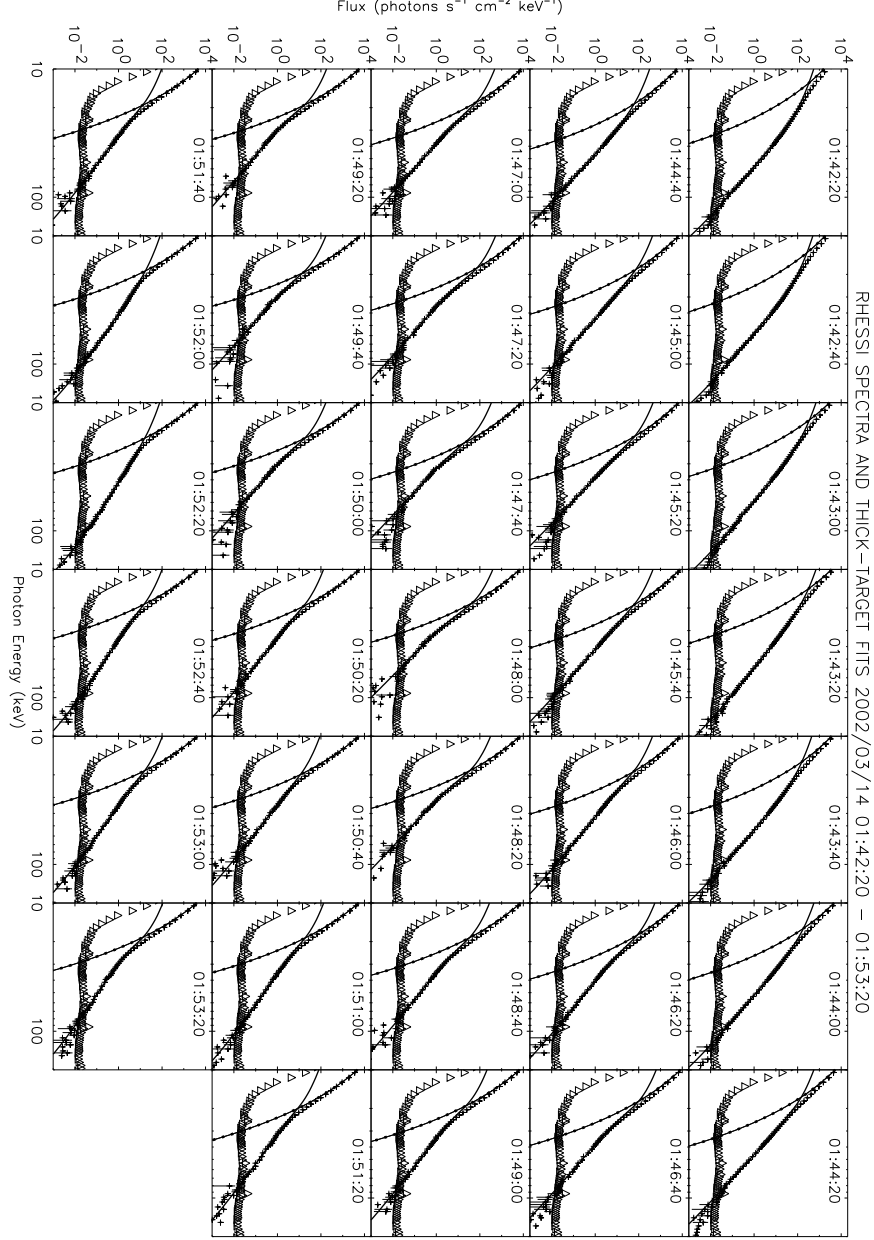
Fig. 14.— Thick-target model fits to the RHESSI spectra, 10-200 keV. Fits to the photon spectra were obtained in 20-s time bins from 01:42:20 to 01:53:20. The crosses show the photon fluxes and their associated error bars, and the triangles show the background determined for the flare. The parabolic-shaped curves show the thermal component of the model, and the bent, solid curves show the non-thermal component, which is the bremsstrahlung flux from a thick target produced by a broken power-law electron energy spectrum. As discussed in the text, there are 5 variable parameters and 3 constant parameters in the model.
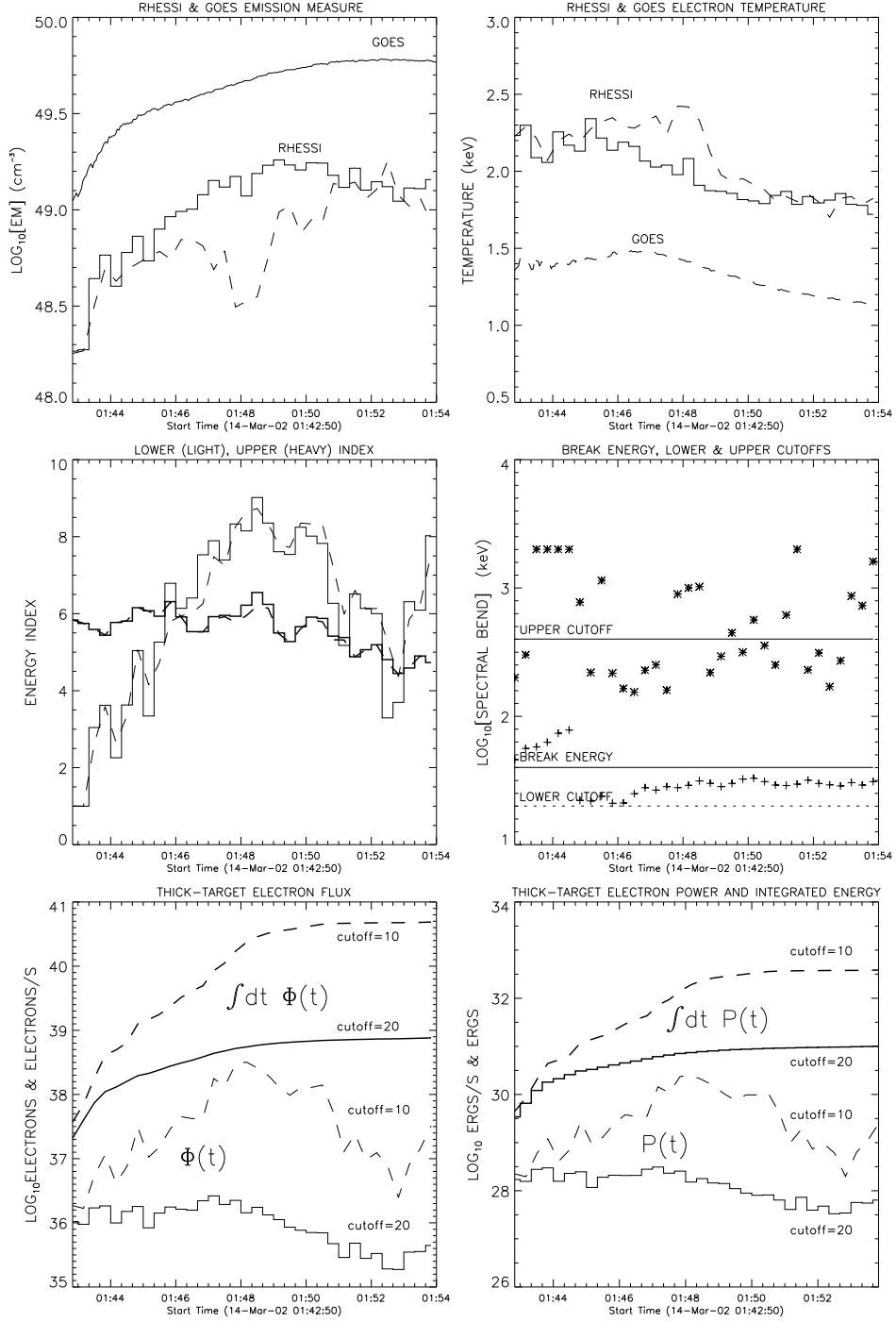
Fig. 15.— Electron distribution parameters from thick-target model. In all panels the dashed curves are for a model with a 10-keV cutoff, and solid curves are for a 20-keV cutoff. In panel #5, the electron flux (s^{-1}) in the thick target is shown by the lighter curves, and the time-integrated flux is shown by the heavier curves. Similarly in panel #6 for the electron power and time-integrated energy.